A study of process-induced grain structures during steady state and non-steady state electron-beam welding of a titanium alloy

Yu Lu[a,*], Richard Turner[a], Jeffery Brooks[a], Hector Basoalto[b]

[a] School of Metallurgy and Materials, University of Birmingham, Birmingham, B15 2TT, United Kingdom

[b] Department of Materials Science and Engineering, The University of Sheffield, Mappin Street, Sheffield, S1 3JD, United Kingdom

[*]Corresponding author.

E-mail address: y.lu.2@bham.ac.uk (Y. Lu).

Abstract

A detailed microstructural characterisation of the emerging weld-line grain structure, for bead-upon-plate welds in Ti-6Al-4V (Ti64) of differing plate thickness, was performed. The microstructure studied was formed during both steady state and non-steady state sections within the weld path, with the non-steady state portion being taken from the end of the plate as the weld bead and heat source overhang the edge of the plate. This allows for the effects of welding process conditions on the microstructural evolution to be determined. The weld pool geometry and 3D tomography of the weld-induced defects have been investigated. Detailed characterisation of microstructure and texture for different welding parameters and for steady and non-steady states have been used to identify physical parameters for the microstructure predictions that are difficult to obtain otherwise. The different states significantly affect the weld crown shape and formation, weld toe, weld bead depth and width. However, the heat affected zone (HAZ) remains unchanged. Regarding the microstructural evolution, both the steady and non-steady states have similar microstructure and texture. No defects were observed in the steady state section of welds, but sub-surface spherical pores have been observed in the non-steady state section of a weld. Finite element modelling to simulate the thermal-metallurgical-mechanical fields within the steady and non-steady state sections of the welds was considered, and the cooling rates predicted within steady state and non-steady sections were interrogated to improve the theoretical understanding of the microstructure and defect formation differences in these Ti64 EB weld regions.

1. Introduction

Titanium (Ti) alloys have been widely used in aerospace and automotive industries because of their high strength-to-weight ratio and superior corrosion resistance at room temperature and elevated temperatures. Titanium exists in two allotropic phases, hcp structured α phase and bcc β phase. By properly alloying certain chemical elements, α, near α, α-β, near β and β alloys can be produced. Ti-6Al-4V is the most common titanium α-β alloy due to its good strength coupled with good fabricability [1]. Aluminium (Al) is added to the alloy as the α-phase stabilizer and hardener due to its solution strengthening effect. Vanadium (V) stabilizes the ductile β-phase, providing hot workability of the alloy.

To fabricate complicated Ti64 components for automotive parts, satellite launch vehicles and aircraft turbine engines, a high-quality, high-integrity welding technique is required. Welding methods for titanium alloys are complicated due to their very reactive nature with atmospheric gases like oxygen, nitrogen, carbon or hydrogen above 550 ℃, particularly when the alloy is molten, which can cause severe embrittlement. In order to avoid contamination of the fusion and heat affected zone of the weld with atmospheric gases, electron beam welding (EBW) techniques have been introduced [2]. The EBW process is carried out inside a high vacuum chamber which shields the hot metal from contamination by oxygen. It is a fusion welding process that utilizes electrons as a source of energy, focusing a stream of electrons using magnetic fields to act as an external heating source which is used to join the metallic components. EBW is a highly efficient and precise technique that is being used increasingly in industrial manufacturing engineering [3,4]. Another significant advantage of electron beam welding is the ability to make deeper and narrower welds compared with other conventional welding methods such as arc welding. Due to the focused beam, it offers lower heat input to the weld than arc welding methods, resulting in low distortion in components. EBW is a complex process with a considerable number of operating parameters defining the electron beam welding operation (accelerating voltage, beam current and welding speed etc.) and thus determining the weld quality and integrity.

The microstructural evolution and phase transformation that occur during the EBW process are important as they can significantly affect the integrity of the welds. Some studies on the microstructure and mechanical properties of the EBW Ti64 alloys have been reported. The welding technique and its effects on thick Ti64 alloy (~20 mm) have been investigated [5]. The microstructure and mechanical properties of EBW post-weld heat treated Ti64 have been examined [6]. The formation of the heat affected zone (HAZ) of an EBW in Ti64 has been discussed [7]. Bahu et al. have studied the effect of beam oscillation on the subsequent fatigue life of Ti64 electron beam welds [8]. The effects of the heterogeneity in the electron beam welded joints on fatigue crack growth in Ti64 alloys have been studied [9]. Wang et al. have proposed that different beam scanning patterns affect the microstructure and mechanical properties of EBW Ti64 [10]. Rao et al. have investigated the fracture toughness of two and three pass bead-over-bead (BoB) EBW Ti64 [11]. Regarding the defects in the titanium welds, several studies have been carried out. The mechanism of porosity formation during the fusion welding of CP-Ti has been provided [12]. Kar et al. have found the relationship between the beam oscillation, porosity formation and fatigue behaviour of EBW Ti64 [13]. However, little research has been reported concerning the process-induced grain structure and porosity during steady state and non-steady state of electron beam welding of Ti64 alloy.

In this study, Ti64 plates with different thicknesses (1 mm, 4 mm and 5 mm) were electron beam welded. A comprehensive characterisation of the steady and non-steady states within each weld has been conducted including weld pool geometry, microstructure and 3D tomography of defects. An improved understanding of the characteristics of the welds, their mechanical properties and microstructural features, represents an important step in the development of a reliable and repeatable production of defect-free EB welds made for industry application, which have been fully characterised.

2. Theory and modelling

In order to compare the thermal effects of the welding process for different welding process parameters (beam power, travel speed) and for different plate thicknesses, an analytical model is required. The energy per unit length term, commonly used in fixed welding thicknesses, is not adequate, and thus needs amending to take into

consideration the geometry. A descriptive parameter to quantify the energy density, namely the penetration depth caused by a beam in a given geometry, is required, which accounts for all of the electron beam, material and plate geometry variations. Relevant literature was consulted [14-16] to understand the proposed analytical solutions to this field. Such a parameter is more commonly used by weld engineers to determine the beam current (and hence the beam power) to achieve a required weld depth. Thus, the current I is typically the subject of the equations. However, a simple re-arrangement can allow for the depth to be made the subject, depending upon the various process and geometry parameters. The Zuev model [15], which is based upon an energy balance in the molten zone, can be re-arranged to yield Eq. (1).

$$H = \frac{P}{v} \cdot \frac{4\eta_{\mathrm{eff}}\eta_{\mathrm{t}}d}{\pi B_{\mathrm{mean}}^2 \rho (cT_{\mathrm{m}} + L_{\mathrm{m}})} \qquad (1)$$

where P is the beam power ($I \cdot V$), v is the travel velocity, η_{eff} and η_{t} are the effective and thermal efficiencies, d is the EB diameter, B_{mean} is the mean weld bead width, ρ is the density, c is the specific heat capacity, T_{m} is the melting temperature (K) and L_{m} is the latent heat of fusion. A primary disadvantage of the Zuev method is the need for a-priori knowledge of the pool width, and very difficult to determine efficiencies.

Finite element models were created to simulate the steady state and non-steady state thermal conditions of an electron-beam weld, to further understand the associated cooling rates at different locations within the plate. The steady-state is assumed to be simulated as the weld pool traverses uninterrupted along the continuum of the plate, whilst the non-steady state occurs as the weld pool leaves the plate at the edge, thus only partially over-hanging the plate. FE models were computed using the specialist welding software Sysweld, from ESI-Group. A material file representing the Ti64 alloy, containing temperature-dependent tabular data for the thermal conductivity, specific heat capacity, Young's modulus, was collated. A small section of plate, large enough to allow for steady-state weld bead formation and travel, was discretized with a graded mesh consisting of hexahedral (brick) elements measuring 0.2 mm × 0.16 mm × 0.5 mm at the weld line. A double ellipsoidal (so-called Goldak) heat source [17] was used to represent the distribution of heat caused by the travelling EB source in the plate, whereby the Goldak function is described in Eq. (2).

$$q(x, y, z, t) = \frac{6\sqrt{3}f_i \eta Q}{a_i bc\pi\sqrt{\pi}} \exp\left(-\frac{3x^2}{a_i^2} - \frac{3y^2}{b^2} - \frac{3z^2}{c^2}\right) \quad \text{for } i = \{\text{front, rear}\} \qquad (2)$$

where $q(x, y, z, t)$ is the spatial and temporal power density, a_f and a_r are the front and rear sector radii, b and c are the radii in the width and height planes, Q is beam power, η is efficiency, and f_f and f_r are the proportions of energy in the front and rear quadrants, where $f_f + f_r = 2$. The applicability of the double ellipsoid equation for heat sources in thin plate beam welds is reported in the literature [18].

3. Material and methods

The Ti-6Al-4V plates were supplied by Ti-Tek UK Ltd., Birmingham. The chemical composition (in wt.%) of the alloy is Al-6.24, V-3.96, C-0.018, Fe-0.003, O-0.072, N-0.007, H-0.0025, Ti-balance. The autogenous bead-on-plate electron beam welding was performed at Bodycote using different Ti64 plate thicknesses and the welding conditions are shown in Table 1. The welds were traversed with constant power and speed, across the entire length of the plate. Thus, the majority of the weld line is performed with a steady-state weld pool. However, the weld pool must "overhang" the edge of the plate at the free-edges of the plate at the beginning and end, thus the rear and the front portions of the ellipsoidal heat source have to be linearly redistributed accordingly at the start and the end respectively. Hence, for these short sections of weld, of length less than the steady-state weld pool length, the heat source is non-steady. Non-steady pools were examined at the midpoint in the non-steady weld portion.

To predict the penetration depth of each of the steady-state 1 mm, 4 mm and 5 mm plate welds considered in this work, during the steady state of the EB welds, analytical calculations using the Zuev, Hashimoto and Lopatko equations were performed, using the relevant material and beam parameter values. These predictions are given in Table 1. Note that if a predicted weld penetration exceeds the plate, this simply means the beam would be predicted to be fully penetrating.

Table 1 Experimental matrix and analytical penetration depth predictions for the EB welds.

Sample No.	Plate Thickness (mm)	EB Power (kW)	Travel Speed (mm/s)	Zuev penetration H_Z (mm)	Hashimoto penetration H_H (mm)	Lopatko penetration H_L (mm)

1	1.0	0.56	25	1.15	2.16	1.28
2	4.0	3.10	25	3.18	9.17	4.84
3	5.0	3.10	25	2.73	9.17	4.84

The samples were machined from the different areas of welded plates, as shown in Fig. 1. The yellow rectangle indicates the steady state section taken from the middle area away from the start and finish of the weld. The red rectangle indicates the non-steady state section taken from the end of the plate.
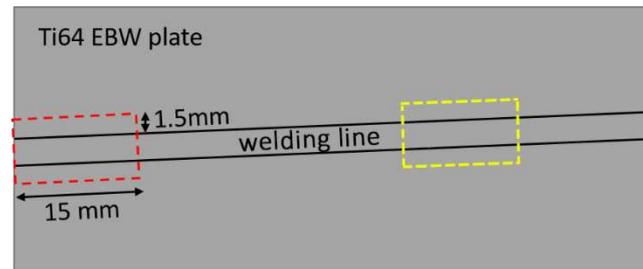
Fig. 1. Schematic illustration of specimen cutting from the EBW Ti64 plates.

The welded Ti64 plates were sectioned transverse to the weld direction and polished for metallurgical examination. The metallography specimens were polished down to 0.04 µm and then etched in a solution containing 2 mL HF (hydrofluoric acid), 10 mL HNO$_3$ (nitric acid) and 88 mL distilled water. The respective optical micrographs for each welding condition were captured using a Zeiss Axioskop 2 MAT optical microscope facility. Image J and Photoshop software were used to analyse the weld pool dimensions and grain size. The grain size was calculated using the planimetric method according to ASTM E112-12 standards. The schematic drawing shows the locations of the weld pool dimensional measurements in terms of the different parameters used, including the crown width, toe width and HAZ width (Fig. 2).
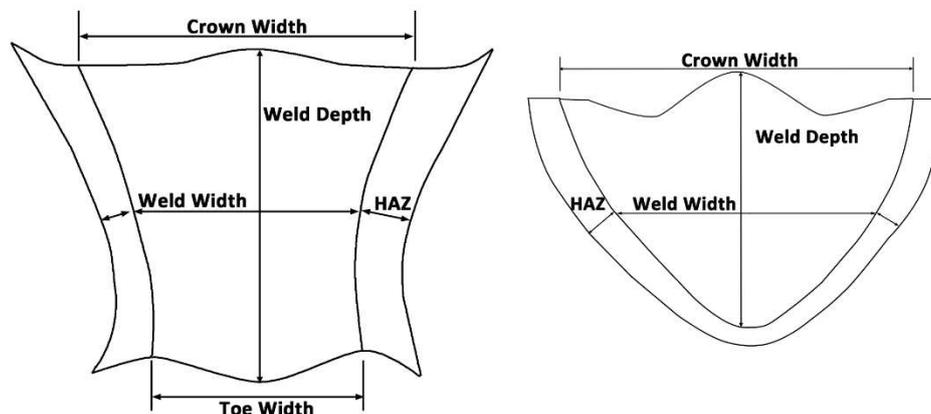
Fig. 2. Schematic drawings to show the dimensional measurements of weld pool.

To reveal the evolution of the microstructure and texture during welding, the cross-sections of the welds were examined by a scanning electron microscope (SEM) and electron backscatter diffraction (EBSD). An SEM JEOL JSM-7000F was operated at 20 kV. HKL Channel 5 software was used to do the EBSD data acquisition and analysis. To ensure a good surface quality of the test samples for EBSD measurements, the samples were subjected to extensive final polishing.

X-ray computed tomography (MicroCT) scanning analysis methods were performed to gain high-resolution 3D images of the Ti64 welds. The scans were carried out at 170 kV and 70 µA. Avizo software was used to reconstruct the 3D volume and thus provide the 3D material characterisation.

A Deben CT5000 micromechanical testing machine was used for tensile loading with the testing conducted on flat dog-bone tensile samples with 2 mm width and 5 mm length gauge.

4. Results

4.1 Weld pool characterisation

Clean and uniform weld beads were obtained in EBW Ti64. The steady state welds were generally quite stable due to the absence of dynamic starting or ending effects associated with the pool growing or shrinking. The transverse sections for steady-state were taken away from the usual end effects that occur at the start and finish of the weld. Fig. 3 shows the weld pool cross-section variations of steady state and one instance of non-steady state which containing fusion zone (FZ), heat affected zone (HAZ) and base material (BM). Sample 1 is fully penetrating the 1 mm thick plate, while Samples 2 and 3 are partially penetrating through the 4 mm and 5 mm plates during the welding. The same penetration of welds was found in the non-steady state weld cross-sections.
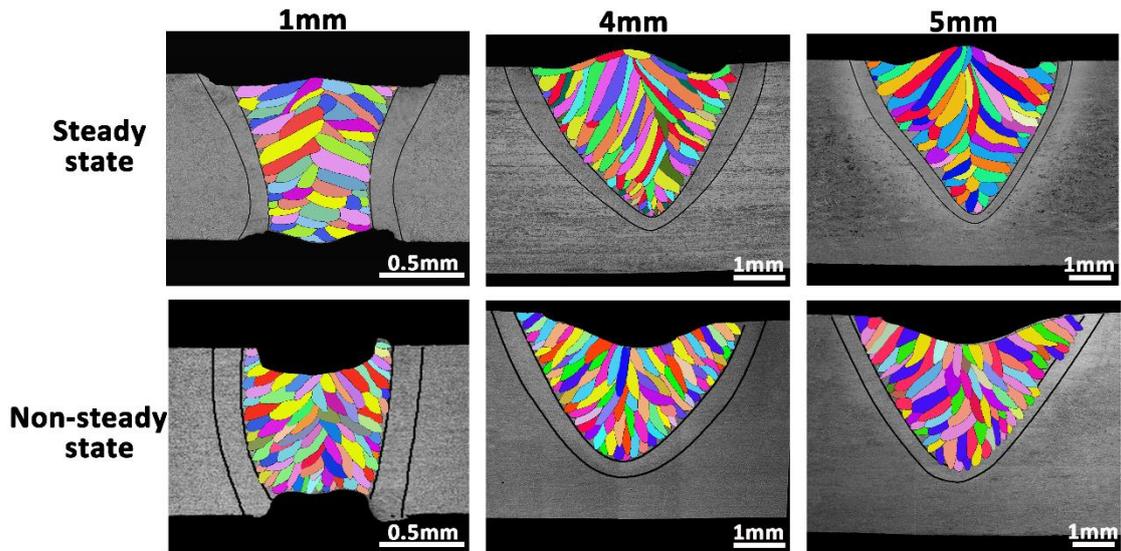
Fig. 3. Metallographic cross-sections of Ti64 with different energy per unit area during electron beam welding: steady state and non-steady state.

The geometry characteristics of the welds are summarized in Table 2. The weld depth measurements include the additional depth caused due to the formation of the crown and toe. It can be seen that Sample 1 (steady state) has a smaller crown width, HAZ, weld width and weld depth. It has been found that the welds at steady state have larger weld depth and smaller weld width when compared with the non-steady state welds. However, the size of the HAZ is similar for both steady and non-steady states. It is shown that the smallest grain size is in Sample 2 (steady) and Sample 1 (non-steady), 170 µm and 70 µm, respectively. The non-steady state sections of welds have smaller grain sizes in the FZ when compared with their equivalent steady state samples.

Table 2 Weld characteristics of EBW Ti64.

	Sample thickness (mm)	Crown width (mm)	Weld width (mm)	Toe width (mm)	HAZ (mm)	Weld depth (mm)	Grain size in FZ (µm)
Steady state	1	1.01	0.62	0.67	0.13	0.98	197
	4	4.25	2.64	-	0.37	4.02	170
	5	4.56	2.71	-	0.38	4.47	233
Non-	1	0.89	0.81	0.60	0.16	0.72	70

steady state	4	4.53	2.92	-	0.39	3.09	110
	5	4.87	3.06	-	0.38	3.45	130

Comparing the measured pool depths with the various models for predicting steady-state energy dissipation into the plates, it becomes evident that the Lopatko and the Zuev models are the closest matchings to the experiment. They both correctly predict full penetration of the 1 mm plate, whilst the Lopatko model marginally over-predicted pool depth for the 4 mm and 5 mm plates (by 0.3 to 0.5 mm), whereas the Zuev model under-predicts the pool depth for the 4 mm and 5 mm plates by a slightly larger margin (roughly 1 mm too shallow). However, as analytical models, they both sit within typical modelling prediction tolerances.

The FE modelling framework was interrogated to understand the change in cooling rates at the weld line and surrounding material, for the steady state central part of the weld line compared with the transient effects as the weld bead leaves the edge of the plate. A 'cooling zone', namely the solidifying molten weld pool and surrounding heated material, is identified in the model by considering negative temperature rates. Fig. 4 illustrates a comparison of cooling rates during steady state and a transient result taken as the weld bead exits the edge of the plate, for both 1 mm thickness and 4 mm thickness plates. Clearly, the cooling rates increase throughout the non-steady state part of the weld line, however, a peak value of this cooling rate at the weld line for each plate thickness is presented in Table 3, to show how different this value is when compared with the weld line at steady state.
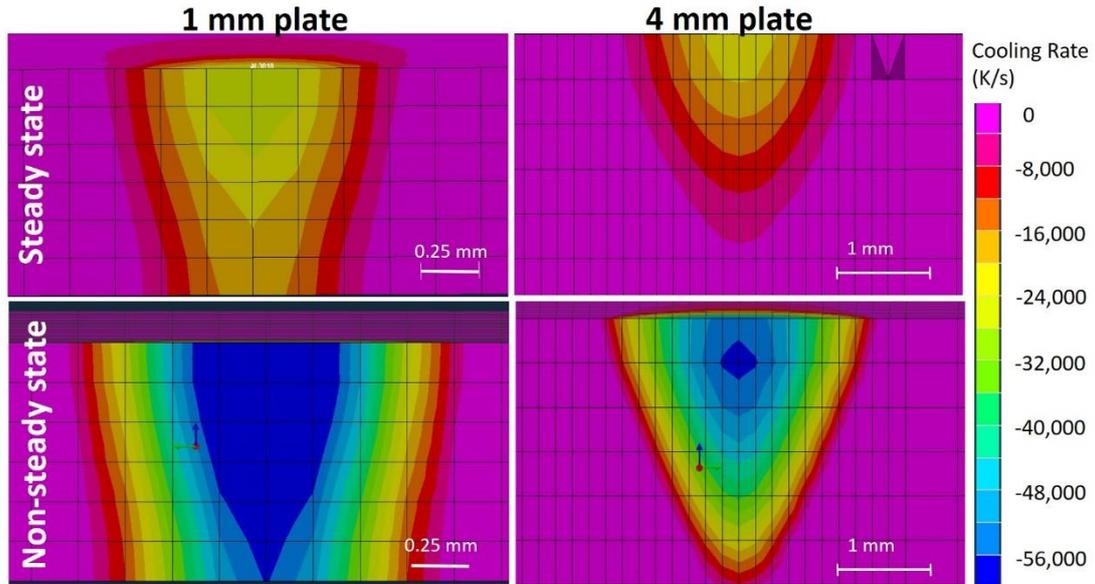
Fig. 4. Cooling rates experienced by steady state welding and one instance of transient results from non-steady section.

It can be observed from the modelled predictions that the cooling rates are highest for the thinnest plate, due to the increased surface area to volume ratio. Additionally, the increase in cooling rate experienced during the non-steady state end of a welding pass is considerable for all plate thicknesses, peaking at around 2½ times greater than during the steady-state welding, as the molten material approaches and breaks through the free-end surface of the plate. This significant change in cooling rate can have a notable impact on the absolute temperature reached which in turn will influence the thermal strain observed in the weld, based upon the fundamental relationship of thermal strain, $\alpha_{\mathrm{L}} = \frac{1}{L}\frac{\mathrm{d}L}{\mathrm{d}T}$, whereby L is length, and T is temperature. The significant change in cooling rate will also affect the microstructure formed given the role cooling rate plays in determining volume fraction and size of the primary α phase [19].

Table 3 Cooling zone width and peak cooling rates experienced in steady state and non-steady state 1 mm, 4 mm and 5 mm plate welds.

Sample thickness (mm)	Steady state		Non-steady state	
	Cooling zone width (mm)	peak cooling rate (K/s)	Cooling zone width (mm)	peak cooling rate (K/s)
1	1.25	28,000	1.65	70,000

4	2.80	20,000	3.25	58,000
5	2.70	12,000	3.65	28,000

4.2 Microstructure

Microstructures of BM, HAZ and FZ for the steady and non-steady states are given in Fig. 5. The microstructure characterisation of the weld cross-sections shows the significant transition that occurs from slightly equiaxed (in the BM) to an acicular microstructure (in the FZ). This variation is because of melting of the base material during welding and the subsequent cooling with a different cooling rate. The FZ, where Ti64 had melted during the welding operation, consists of coarse columnar β grains of ~200 μm at steady state and ~100 μm for non-steady state. The columnar grains in the FZ are nucleated from the unmelted β grains near the HAZ, and grow preferentially along the β<100> orientation closest to the maximum temperature gradient direction [20,21]. The microstructures in the FZ are characterized by a fully β transformed structure in the presence of martensitic α′ in needle-shape formations. The β phase forms on cooling from the liquid, and subsequently transforms to the acicular α′ during rapid cooling to below the β transus. The width of fine lamellar martensitic α′ in the FZ is several hundred nm. The HAZ and BM exhibit finer grains. The phase transition between the HAZ and BM is shown in Fig. 5. The ghost α phases, observed in the HAZ, are former primary α phases of the BM which transform into the β field during welding, but time and temperature are not sufficient to reach chemical equilibrium (solid solution of β phase). The microstructure of the BM consists of large-aspect ratio elongated α grains along the rolling direction from the initial manufacturing route. The above observations can also be found in all the non-steady state welds.
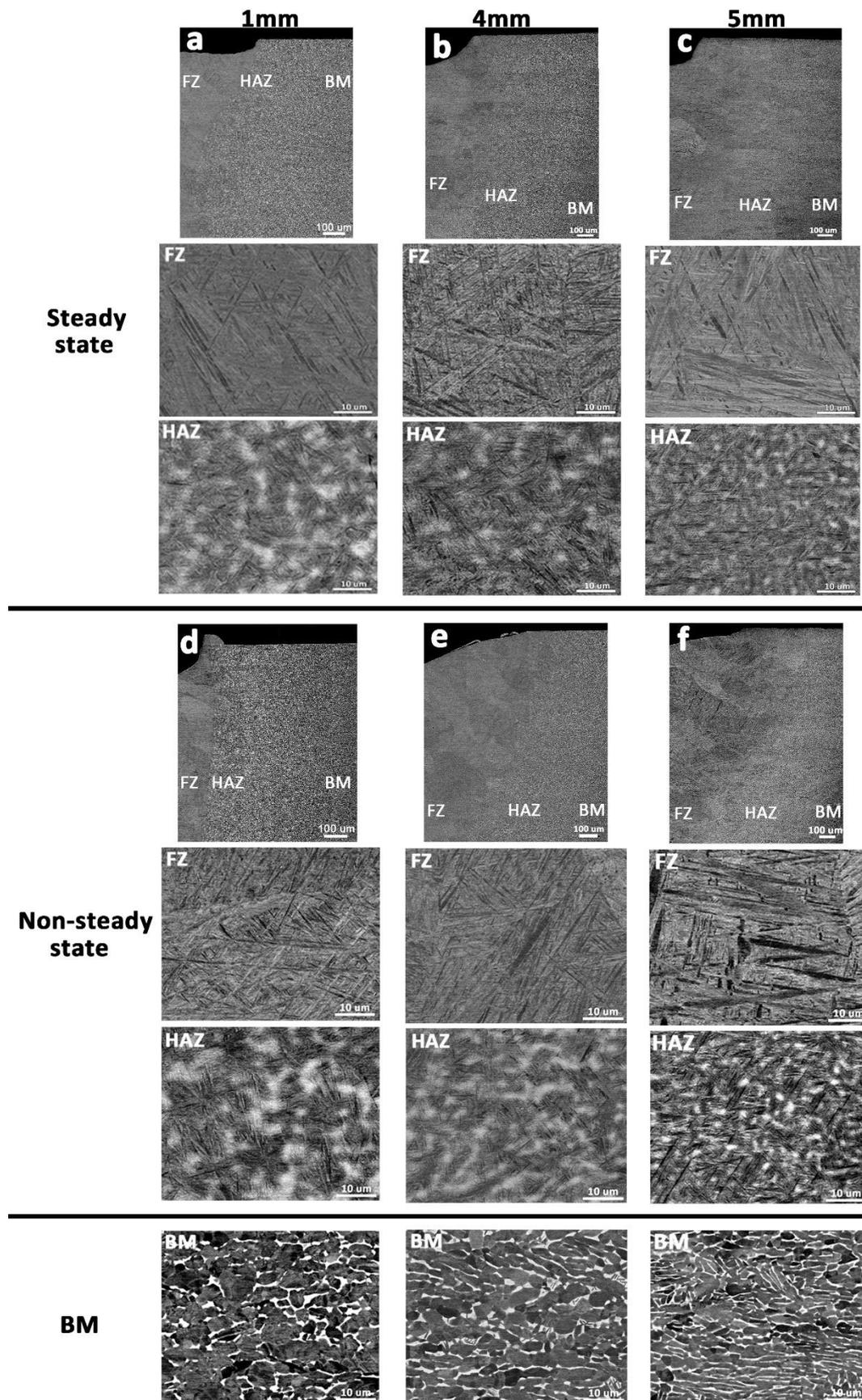
Fig. 5. SEM images of EBW Ti64 taken from different locations (FZ, HAZ and BM): (a, d) 1 mm plate, (b, e) 4 mm plate, (c, f) 5 mm plate.

Fig. 6 shows representative inverse pole figure (IPF) maps obtained from the cross-sections of the EBW Ti64 samples. In the maps, individual grains are coloured according to the crystallographic orientations relative to the rolling direction (RD), and the colour legend is shown. The fine martensitic α' microstructure is shown in the FZ of both steady and non-steady states. The BM shows the presence of some preferential crystallographic orientations especially in the thinner sample (Fig. 6(m-o)), also called macrozones, which are often detected in rolled or forged Ti alloys where partial recrystallization takes place, resulting in microstructural and crystallographic orientation heterogeneities [22]. The {0001} pole figure indicated that the BM has a typical rolling texture with the basal planes tilted away from the normal direction (ND) to the transverse direction (TD), which is typical for hot-rolled Ti plates. The formation of a basal texture has been reported in Ti alloys deformed by hot rolling [23].
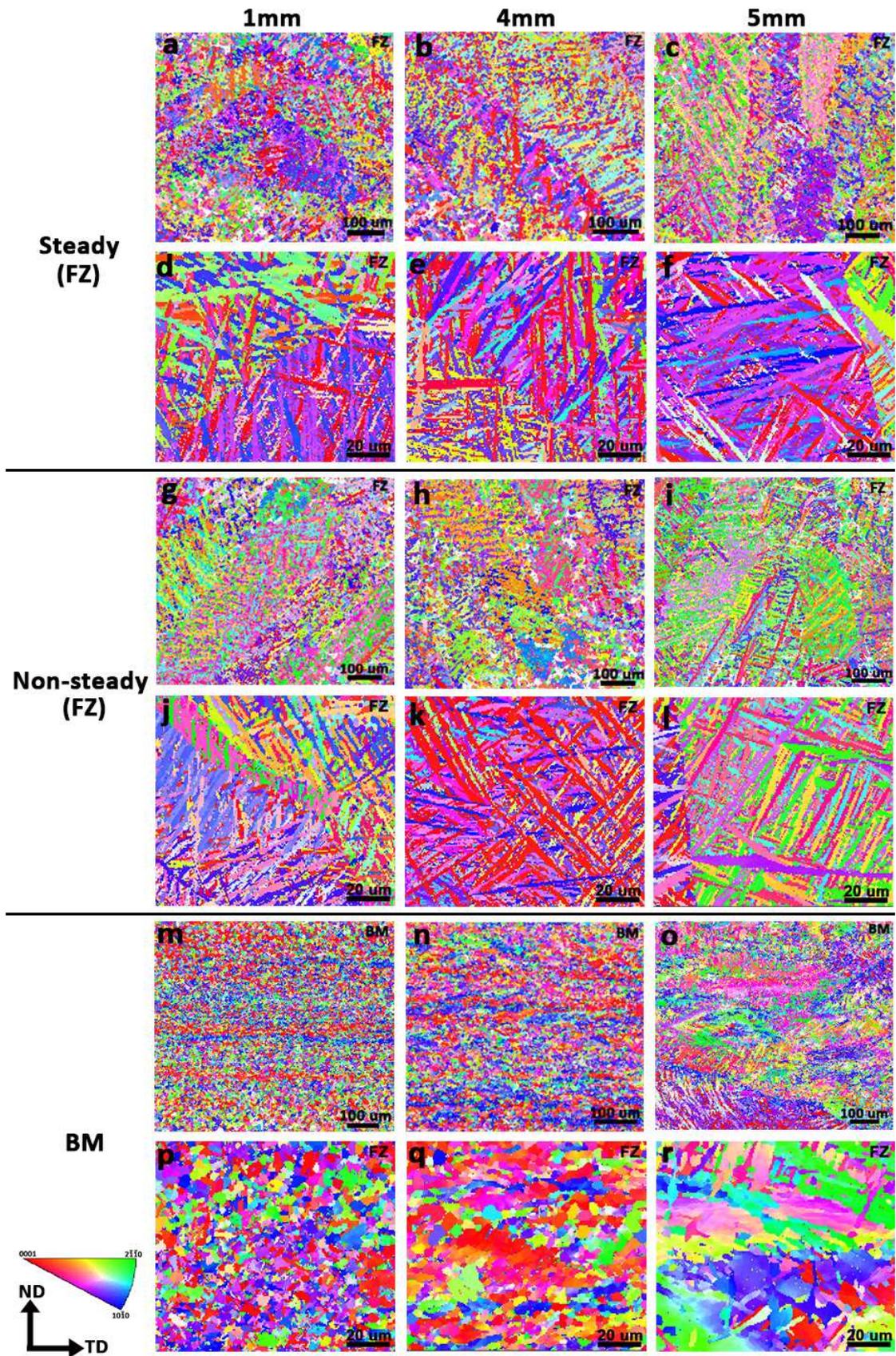
Fig. 6. IPF maps of cross-sections of EBW Ti64 welds in FZ of steady and non-steady states and base material: (a, g, m) 1 mm plate, (b, h, n) 4 mm plate, (c, i, o) 5 mm plate. (d-f), (j-l), (p-r) show the higher magnification of IPF maps in different zones.

The $\{0001\}_\alpha$ and $\{10\bar{1}0\}_\alpha$ pole figures measured from the FZ and BM are shown in Fig. 7. It can be seen that the intensity of the $\{0001\}$ basal plane is significantly higher than that of the prismatic $\{10\bar{1}0\}$ planes. For the steady state part of welds, the relatively higher texture intensities of the FZ are examined in the thicker plates (4 mm and 5 mm). Comparing with the steady state sections, the samples from the non-steady state sections have similar textures. The textures in the BM have more preferred orientation than textures in the FZ. The BM has a typical rolling texture with basal planes tilted about 20°-40° from the normal direction (ND) towards the transverse direction (TD), as shown in Fig. 7(g). This texture is frequently found when deformation was performed at a temperature where the α phase is the main contributor to the deformation [24,25]. The *c*-axis tends to be parallel to either the RD or the ND in 1 mm BM (Fig. 7(g)). Similar tendencies can be seen in the 4 mm and 5mm BM, but with higher intensity (Fig. 7(h) and (i)).
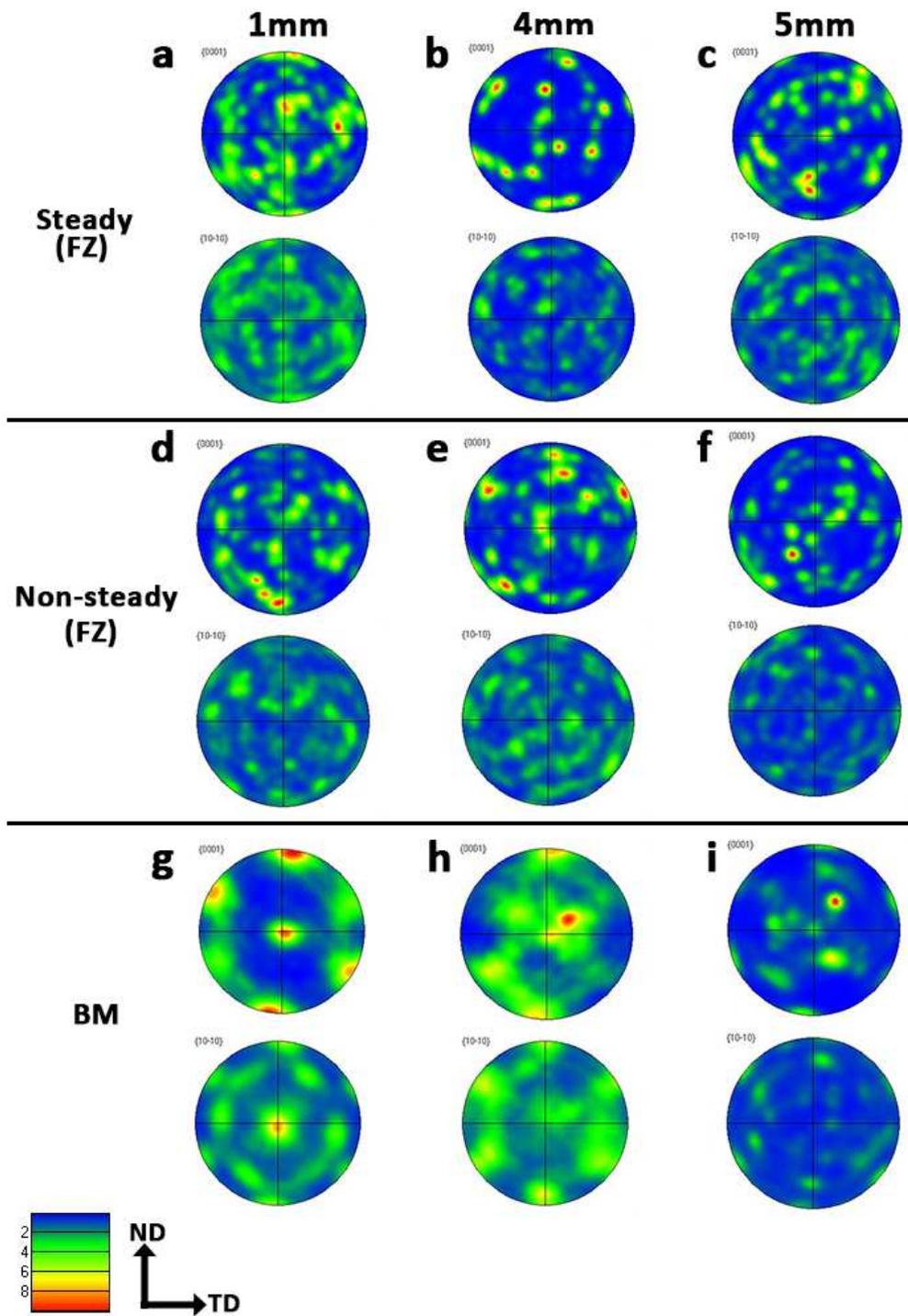
Fig. 7. {0001} and {10$\bar{1}$0} pole figures corresponding to the different regions (FZ and BM): (a, d, g) 1 mm palte, (b, e, h) 4 mm plate, (c, f, i) 5 mm plate.

4.3 Micro-CT tomography

Fig. 8 illustrates the 3D image reconstructions from X-ray tomography of the welds. It is evident that no defects such as micro-cracks, cavities and pores were detected for the steady state weld sections of 1 mm, 4 mm and 5 mm plates (Fig. 8(b, f, j)). When

using X-ray tomography for the non-steady state weld sections, the sub-surface pores were observed (indicated by arrows), as shown in Fig. 8(d, h, l). It is clear that the pores were spherical and in the range of between 120 µm and 310 µm diameter, and were commonly located near the fusion boundary. The presence of pores in the non-steady state weld is due to the unstable thermal fluid flow and the collapse of the liquid to form a depression upon beam power variation. The non-steady thermal cycles lead to sudden increases in high energy density which promote a larger weld pool that is more prone to processing-induced porosity.
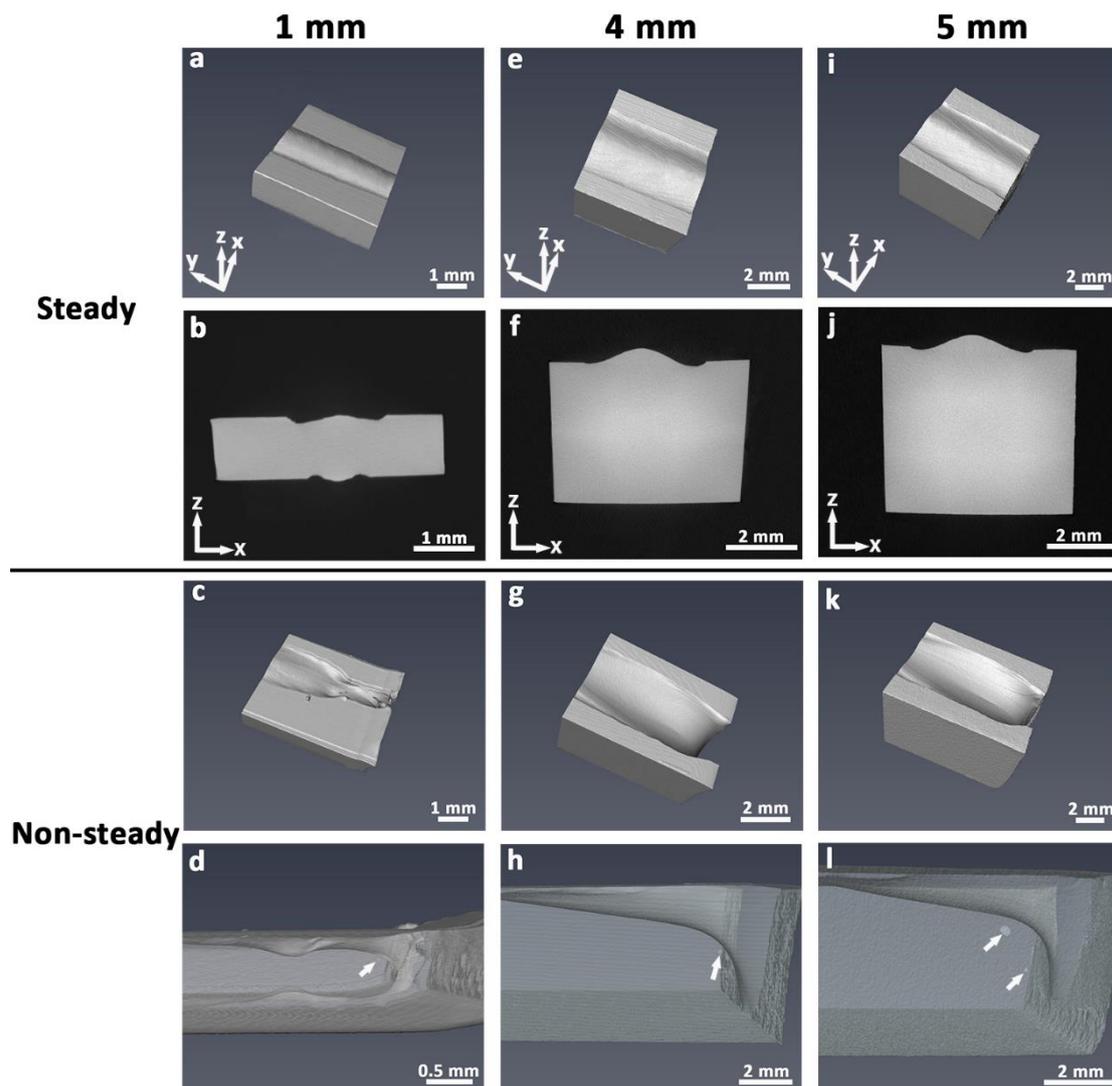
Fig. 8. (a-d) Sample 1 (1 mm); (e-h) Sample 2 (4 mm); (i-l) Sample 3 (5 mm). (a, e, i) Reconstructed 3D X-ray tomography of steady state welds. (b, f, j) Longitudinal sections illustrating the weld shape and absence of pores in the steady state welds. (c,

g, k) Reconstructed 3D X-ray tomography of non-steady state welds. (d, h, l) 3D rendering of non-steady state welds showing porosity.

4.4 Tensile testing

The measured tensile properties of the EBW Ti64 weld line samples (1 mm, 4 mm and 5 mm), welded at steady state, are listed in Table 4. The yield strength and UTS of the base material (Ti64) are 850 MPa and 930 MPa, while the elongation-to-failure is 12%. The highest yield strength and UTS of weld bead material were obtained in Sample 2, which also displays the best elongation-to-failure. Compared with the base material, it is more difficult for EBW welds to deform during tensile loading because of the solidification columnar structure.

Table 4 Tensile properties of EBW Ti64.

Sample	Yield strength (MPa)	UTS (MPa)	Elongation (%)
1	775±12	1072±7	4.0±0.8
2	885±8	1145±10	7.6±1.1
3	840±9	1090±11	5.4±0.9

The fracture surfaces of the EBW Ti64 weld line samples in the steady state are shown in Fig. 9. The welding fusion zone of the EBW samples is located in the centre of the gauge length of the tensile sample. All fractured samples showed dimples on the fracture surface. The fracture surface presents the characteristics typical of ductile failure. The morphology of the dimples varies between the samples and relates to the degree of ductile deformation before the failure. The larger dimples are associated with the larger grain size [26,27]. The dimple size shows a relationship with the strength: the finer the dimple size, the higher strength and ductility [28].
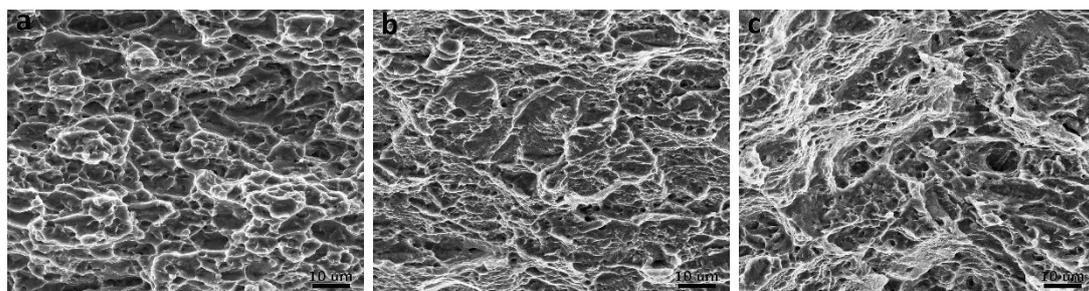
Fig. 9. Fracture morphologies of EBW Ti64 welds after tensile testing at room temperature: (a) Sample 1 (1 mm); (b) Sample 2 (4 mm); (c) Sample 3 (5 mm).

5. Discussion

Due to the selection of appropriate welding parameters, clean and uniform electron beam weld beads were produced in the Ti64 material. As shown in Fig. 3, the weld pool geometries are significantly different between the steady state and non-steady state cross-sections. The induced cooling rates predicted within a specified plate thickness show significant variation in the steady and non-steady sections of weld (Table 3). The non-steady regions also display a slightly wider zone of high cooling rate on the top surface of the plate compared with the steady state. These variations in cooling rates cause the weld pool size to alter accordingly. Comparing with the steady state welds, non-steady state welds have shallower and wider weld pool shapes. However, the width of the HAZ is similar for both steady and non-steady states.

The HAZ width is defined as the width of the region of material where the ghost structure which originated from the β→α transformation is observed. In this region, the phases are far from the equilibrium state because of the rapid thermal processing, which results in insufficient time for full diffusion of the Al and V at the α/β interface. The similar HAZ width for a given weld is believed to be due to the microstructure being unaffected in both steady state and transient conditions. Moreover, the non-steady state welds have a smaller grain size in the FZ compared with the steady state, because they are predicted to have a considerably higher cooling rate gradient (Table 3). The lower cooling rates imply a longer time at temperature and therefore favour grain growth. Upon cooling, the α phase precipitates from the β phase by nucleating at the β grain boundaries. The α phase grows in a lamellar fashion into the interior of the β grains whilst its final length is restricted by the prior β grain size. In addition, the width of lamellar platelets in 5 mm weld plate is larger than that of 1 mm weld plate (Fig. 5). The widths of the lamellar platelets are controlled by diffusion [29], hence coarsening occurs when the cooling rates are slower.

Similar microstructure and texture have been found in both steady and non-steady states (Figs. 5-7). The very fine martensitic α′ microstructures are clearly shown in the FZ of the steady and non-steady states, because of the high cooling rate experienced. The HAZ of the EBW joint also undergoes a similar thermal cycle consisting of rapidly rising and falling temperature gradients, which result in the non-equilibrium phase transformed region of fine α in metastable β phase. Such ghost

structures were observed in all the observed HAZ of steady and non-steady state welded samples. These microstructure features were primary α grains before welding, and the associated chemical segregation of the BM remained through the transformation to β phase during the welding as there was insufficient time to reach chemical equilibrium. Regarding the texture evolution, the variant selection during the phase transformation could affect the evolution of texture in FZ. The growth of the columnar grains in the FZ was affected by the temperature gradient, which leads to the solidification texture. According to the crystallographic symmetry relationship of the bcc structure, β has six {110} planes and two <111> directions in each {110} planes. Theoretically, one β grain can generate 12 possible α variants during the phase transformation [30]. The martensitic α′ phases are produced within the parent β with respect to the Burgers orientation relationship during cooling. This is called 'texture memory', which has been reported previously in Ti alloys [31-33]. Therefore, the crystallographic orientations in the FZ of two states are similar, and significantly dependent on the microstructure of the HAZ containing the ghost α phases.

Sample 2 has the highest tensile strength and best elongation (Table 4). The tensile strength of the EBW Ti64 welded samples is significantly influenced by the α lath size and β grain size in the emerging microstructure. Since dislocation slip cannot pass directly from one grain to another, as the grain boundaries act as barriers during dislocation motion, so the finer grains can shorten the slip length, reduce the dislocation slip velocity, and decrease the pile-up of dislocations and stress concentration in the grain boundaries [22,34,35]. Thin martensitic α′ phases provide a poorer medium for energy absorption and limit resistance to crack propagation. The fine scale of the martensitic microstructure in the EBW Ti64 welds results in high strength of the emerging microstructure.

6. Conclusions

The weld pool shape, microstructural observations and measured tensile properties of EBW Ti64 plates - with different thicknesses and different states (steady and non-steady) - have been investigated through detailed characterisation methods. The main findings are as follows:

(1) The weld pool geometries of the two states are significantly different, but the size of the HAZ is similar for both steady and non-steady states. Similar

microstructures were observed in both states: a fusion zone consisting of an acicular martensitic α', a heat-affected zone consisting of a non-equilibrium 'ghost' microstructure of partially dissolved α and base material of lamellar α/β. Compared with the steady state, the non-steady state samples have similar textures in the FZ because of 'texture memory'. Relatively higher texture intensities were observed in the thicker plates (4 mm and 5 mm) at steady state.

(2) Finite element modelling illustrates the significantly higher cooling rates experienced, primarily at the centre of the weld pool, during non-steady state welding. There is also a small increase in the volume of material experiencing these very high cooling rates during the non-steady section of weld line. The non-steady state welds have smaller grain sizes in the FZ compared with the steady state welds, which is attributed to the higher cooling rate.

(3) The X-ray tomography revealed that no defects were formed in the steady state welds, while sub-surface spherical pores were observed in the non-steady welds, caused by unstable thermal fluid flow interactions.

(4) The use of electron beam welding significantly affected the mechanical performance of joints, higher tensile strength and lower ductility were obtained in all EBW Ti64 samples when compared with the base Ti64 material.

References

[1]   R.R. Boyer, Mater. Sci. Eng. A 213 (1996) 103-114.

[2]   N. Saresh, M.G. Pillai, J. Mathew, J. Mater. Process. Technol. 192-193 (2007) 83-88.

[3]   R.C. Reed, H.J. Stone, S.M. Roberts, J.M. Robinson, Proc. Inst. Mech. Eng. Part G J. Aerosp. Eng. 211 (1997) 421-428.

[4]   J. Norrish, Advanced Welding Process-Technology and Process Control, Woodhead Publishing Limited, Cambridge, 2006.

[5] N. Saresh, M.G. Pillai, J. Mathew, J. Mater. Process. Technol. 192 (2007) 83-88.

[6] R. Pederson, F. Niklasson, F. Skystedt, R. Warren, Mater. Sci. Eng. A 552 (2012) 555-565.

[7] S. Zhang, Y. Ma, S. Huang, S.S. Youssef, M. Qi, H. Wang, J. Qiu, J. Lei, R. Yang, J. Mater. Sci. Technol. 35 (2019) 1681-1690.

[8] N.K. Babu, S.G.S. Raman, C.V.S. Murthy, G.M. Reddy, Mater. Sci. Eng. A 471 (2007) 113-119.

[9] X. Li, S. Hu, J. Xiao, L. Ji, Mater. Sci. Eng. A 529 (2011) 170-176.

[10] S. Wang, X. Wu, Mater. Des. 36 (2012) 663-670.

[11] K.P. Rao, K. Angamuthu, P.B. Srinivasan, J. Mater. Process. Technol. 199 (2008) 185-192.

[12] J.L. Huang, N. Warnken, J.C. Gebelin, M. Strangwood, R.C. Reed, Acta Mater. 60 (2012) 3215-3225.

[13] J. Kar, D. Chakrabarti, S.K. Roy, G.G. Roy, J. Mater. Process. Technol. 266 (2019) 165-172.

[14] V.K. Dragunov, E.V. Terentyev, A.P. Sliva, A.L. Goncharov, D.A. Zhgut, IOP Conf. Ser.: Mater. Sci. Eng. 681 (2019) 012011.

[15] I.V. Zuev, Materials Processing by Concentrated Energy Flows, MPEI, Moscow, 1998.

[16] T. Hashimoto, F. Matsuda, J. Jpn. Weld. Soc. 33 (1964) 38-46.

[17] J. Goldak, A. Chakravarti, M. Bibby, Metall. Trans. B 15 (1984) 299-305.

[18] T.F. Flint, J.A. Francis, M.C. Smith, J. Balakrishnan, J. Mater. Process. Technol. 246 (2017) 123-135.

[19] S. Zhu, H. Yang, L.G. Guo, X.G. Fan, Mater. Charact. 70 (2012) 101-110.

[20] S. Kou, Y. Le, Metall. Trans. A19 (1988) 1075-1082.

[21] W.F. Savage, C.D. Lundin, A.H. Aronson, Weld. J. 44 (1965) 175S-181S.

[22] S. Roy, S. Suwas, S. Tamirisakandala, R. Srinivasan, D.B. Miracle, Mater. Sci. Eng. A 540 (2012) 152-163.

[23] S.F. Frederick, G.A. Lenning, Metall. Trans. B 6 (1975) 601-605.

[24] M. Peters, C. Leyens, Titanium and Titanium Alloys: Fundamentals and Applications, Wiley- VCH Verlag GmbH & Co. KGaA, 2003.

[25] G. Lutjering, J.C. Williams, Titanium, second ed., Springer, Berlin Heidelberg, 2007.

[26] M.H. Cai, C.Y. Lee, Y.K. Lee, Scr. Mater. 66 (2012) 606-609.

[27] W. Qin, J. Li, Y. Liu, J. Kang, L. Zhu, D. Shu, P. Peng, D. She, D. Meng, Y. Li, Mater. Lett. 254 (2019) 116-119.

[28] T. Kawabata, O. Izumi, J. Mater. Sci. 11 (1976) 892-902.

[29] A. Shaikh, S. Kumar, A. Dawari, K. Shreyas, A. Patil, R. Singh, Procedia Struct. Integr. 14 (2019) 782-789.

[30] H. Beladi, Q. Chao, G.S. Rohrer, Acta Mater. 80 (2014) 478-489.

[31] G.C. Obasi, S. Birosca, J. Quinta Da Fonseca, M. Preuss, Acta Mater. 60 (2012) 1048-1058.

[32] J.L.W. Warwick, N.G. Jones, I. Bantounas, M. Preuss, D. Dye, Acta Mater. 61 (2013) 1603-1615.

[33] A.A. Antonysamy, J. Meyer, P.B. Prangnell, Mater. Charact. 84 (2013) 153-168.

[34] F.J. Gil, M.P. Ginebra, J.M. Manero, J.A. Planell, J. Alloy. Compd. 329 (2001) 142-152.

[35] R. Filip, K. Kubiak, W. Ziaja, J. Sieniawski, J. Mater. Process. Technol. 133 (2003) 84-89.